Computers & Fluids 39 (2010) 1704–1710

Contents lists available at ScienceDirect

Computers & Fluids

journal homepage: www.elsevier.com/locate/compfluid

Computing the Karhunen–Loève dimension of an extensively chaotic flow field given a finite amount of data

Andrew Duggleby [a,*], Mark R. Paul [b]

[a] Department of Mechanical Engineering, Texas A&M University, College Station, TX 77843-3123, United States
[b] Department of Mechanical Engineering, Virginia Polytechnic Institute & State University, Blacksburg, VA 24061, United States

ARTICLE INFO

Article history:
Received 29 April 2009
Received in revised form 23 May 2010
Accepted 8 June 2010
Available online 16 June 2010

Keywords:
Proper orthogonal decomposition
Rayleigh–Bénard convection
Chaos

ABSTRACT

The use of Karhunen–Loève decomposition (KLD) to explore the complex fluid flows that are common in engineering applications is increasing and has yielded new physical insights. However, for most engineering systems the dimension of the dynamics is expected to be very large yet the flow field data is available only for a finite time. In this context, it is important to establish the amount of data required to compute the asymptotic value of the Karhunen–Loève dimension given a finite amount of data. Using direct numerical simulations of Rayleigh–Bénard convection in a finite cylindrical geometry we compute the asymptotic value of the Karhunen–Loève dimension. The amount of time required for the Karhunen–Loève dimension to reach a steady value is very slow in comparison with the time scale of the convection rolls. We show that the asymptotic value of the Karhunen–Loève dimension can be determined using much less data if one uses the azimuthal symmetry of the governing equations prior to performing a KLD. The Karhunen–Loève dimension is found to be extensive as the system size is increased and for a dimension measurement that captures 90% of the variance in the data the Karhunen–Loève dimension is approximately 20 times larger than the Lyapunov dimension.

1. Introduction

Many open challenges remain in the development of ways to describe, model, and predict chaotic fluid flows [1]. One method proposed by Lumley [2] to study turbulence is to use a Karhunen–Loève decomposition, or proper orthogonal decomposition (POD), to decompose the flow into an optimal set of basis functions. This has led to many discoveries and has increased our understanding of turbulence including the dynamics of streaks and bursting events [3–11], the dynamics of energy transfer [12,13], and the mechanism of drag reduction [14–16]. Recently, this has been extended to many experimental and numerical investigations of more complicated flow fields in engineering applications that are quite different than a typical theoretical investigation of fluid turbulence (cf. [17,18]). An important difference is that the interval of time over which the data is available is often very short. This limiting factor is present in both experimental and numerical studies. It is anticipated that the dimension describing the dynamics of these systems is very large and as a result the short time observations provide only a limited sample of the overall dynamics.

We explore this by computing the Karhunen–Loève dimension with time for a high-dimensional fluid flow field. Our results provide insights for the use of KLD for more complex engineering flow fields where only a finite amount of data is available. Our results show that asymptotic values of the eigenvalue spectrum, eigenfunctions, and dimension for the KLD of a complex flow field can be approximated from finite time observations. We will also show that using the rotational invariance inherent to the problem vastly reduces the amount of data required to compute the asymptotic value of the Karhunen–Loève dimension.

We show this by numerically integrating the time-dependent and three-dimensional Boussinesq equations that govern the fluid motion of Rayleigh–Bénard convection in a shallow cylindrical domain. In particular, we explore the spatiotemporal chaos of the fluid convection rolls that arise when a layer of fluid is heated uniformly from below in a gravitational field. A typical flow field pattern from our numerical simulations is shown in Fig. 1 which illustrates a horizontal mid-plane slice of the domain where red is hot rising fluid and blue is cool falling fluid.

We compute the long-time asymptotic value of the dimension resulting from a KLD using two different approaches given a series of two-dimensional flow field images:

(i) In this approach we apply the standard method of snapshots to a series of two-dimensional flow field images.

* Corresponding author.
E-mail address: aduggleby@tamu.edu (A. Duggleby).

0045-7930/$ - see front matter © 2010 Elsevier Ltd. All rights reserved.
doi:10.1016/j.compfluid.2010.06.007

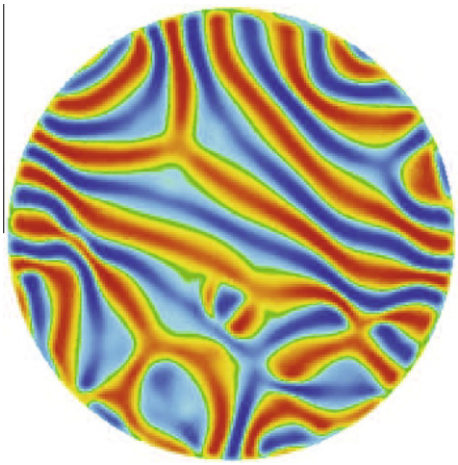

Fig. 1. A typical pattern of convection rolls from a numerical simulation of chaotic Rayleigh–Bénard convection in a shallow cylindrical domain. The flow field is shown at mid-depth $z = 1/2$ where red indicates warm rising fluid and blue indicates cool falling fluid. For this simulation $\Gamma = 10$, $R/R_c = 3.5$, and $\sigma = 1$. (For interpretation of the references to colour in this figure legend, the reader is referred to the web version of this article.)

(ii) In this approach we first take a Fourier transform in the periodic azimuthal direction and then perform the KLD in the radial direction.

In the following discussion we will refer to these directly as Approach (i) and Approach (ii) which are discussed in detail in Sections 2.2.1 and 2.2.2, respectively.

We hypothesize that in the limit of an infinite amount of data the two approaches are equivalent for chaotic flow fields due to the rotational symmetry of the governing Boussinesq equations. For this to be true, every possible rotation of a flow field image must also be realized in time as the dynamics proceed. This is clearly not guaranteed, for example it is well known that nonlinear partial differential equations, such as the Boussinesq equations that govern fluid convection, contain multiple stable solutions when driven far-from-equilibrium. The particular dynamics exhibited will depend upon the specific initial conditions used due to complicated basins of attraction. However, we argue that for large systems exhibiting spatiotemporal chaos these effects will average out and the dimension from the two approaches will be quite similar.

2. Numerical methods

2.1. Direct numerical simulation

The fluid motion of Rayleigh–Bénard convection is governed by the Boussinesq equations

$$\sigma^{-1}(\partial_t \mathbf{u} + \mathbf{u}\cdot\nabla\mathbf{u}) = -\nabla P + \nabla^2\mathbf{u} + RT\hat{z}, \tag{1}$$

$$\partial_t T + \mathbf{u}\cdot\nabla T = \nabla^2 T, \tag{2}$$

$$\nabla\cdot\mathbf{u} = 0, \tag{3}$$

which represent the conservation of momentum, energy, and mass. In our notation ∂_t is a time derivative, $\hat{z}$ is a unit vector in the direction opposing gravity, $\mathbf{u}$ is the fluid velocity, p is the pressure, and T is the temperature. The equations are nondimensionalized using the layer depth d as the length scale, the vertical diffusion time of heat $\tau_v = d^2/\alpha$ for the time scale, where α is the thermal diffusivity, and the constant temperature difference ΔT between the bottom and top plates as the temperature scale. In our investigation we consider a shallow cylindrical convection domain of radius r_0 and depth d. On all material walls we impose the no-slip boundary condition

$$\mathbf{u} = 0. \tag{4}$$

The top and bottom plates are held at a constant temperature $T(z = 0) = 1$ and $T(z = 1) = 0$ and the lateral sidewalls of the domain are perfectly conducting boundaries with

$$T = 1 - z. \tag{5}$$

There are three important nondimensional parameters that completely describe the dynamics. The aspect ratio of the domain

$$\Gamma = \frac{r_0}{d}, \tag{6}$$

which is a measure of the system size and r_0 is the radius of the domain. The Prandtl number

$$\sigma = \frac{\nu}{\alpha}, \tag{7}$$

where ν is the kinematic viscosity, and the Rayleigh number

$$R = \frac{g\beta\Delta T d^3}{\alpha\nu}, \tag{8}$$

where g is the acceleration due to gravity and β is the coefficient of thermal expansion.

The control parameter that is varied in most experiments is R [19]. For no-slip boundaries the critical value of the Rayleigh number is $R_c = 1708$ which corresponds to the onset of convection rolls. For a fluid with $\sigma \approx 1$, as R is increased $R \lesssim 10^4$ the steady convection rolls are replaced by patterns of rolls with time dependent dynamics that include periodic, quasiperiodic, and chaotic dynamics (cf. [20–23]). As R is increased further $R \gtrsim 10^5$ the convection rolls are annihilated and replaced by thermal plume structures yielding turbulent convection [1].

In this paper we are interested in the range where the patterns of convection rolls exhibit spatiotemporal chaos and we use $R = 6000$ (which yields $R/R_c = 3.5$), $\sigma = 1$ and a range of system sizes $6 \leqslant \Gamma \leqslant 15$. In the following we solve the time-dependent Boussinesq equations using a geometrically flexible, efficient, spectral element algorithm [24–26]. Further details on the specific application of this numerical method to thermal convection can be found in Ref. [27].

2.2. Karhunen–Loève decomposition

The KLD of a fluid flow field can be cast as the solution of the Fredholm integral,

$$\int_\Omega K(\mathbf{x},\mathbf{x}')\mathbf{\Phi}(\mathbf{x}')d^3x' = \mu\mathbf{\Phi}(\mathbf{x}), \tag{9}$$

where

$$K(\mathbf{x},\mathbf{x}') = \lim_{\tau\to\infty}\frac{1}{\tau}\int_0^\tau \mathbf{u}(\mathbf{x},t)\otimes\mathbf{u}(\mathbf{x}',t)dt, \tag{10}$$

and $\otimes$ is an outer product, Ω is the volume of the entire domain, $\mathbf{x}$ is the position vector, $\mathbf{\Phi}(\mathbf{x})$ is the eigenvector with associated eigenvalue μ, and $K(\mathbf{x},\mathbf{x}')$ is the kernel. The kernel is built using the two-point correlation of the fluctuating space-time velocity components $\mathbf{u}(\mathbf{x},t)$ averaged over time τ. The Karhunen–Loève dimension D_{KL} is the number of eigenmodes necessary to capture a given fraction f of the total variance of the data

$$\frac{\sum_{j=1}^{D_{\mathrm{KL}}}\mu_j}{\sum_{j=1}^{\infty}\mu_j} = f, \tag{11}$$

where a typical choice is $f = 0.9$. The observation time τ should be long enough such that most of the dynamics on the attractor have been observed. In the limit $\tau\to\infty$ this is satisfied. However, for a finite amount of data it is desired that the data is sufficient for

the dimension to have approached its asymptotic value such that $D_{KL} \approx D_{\infty}$.

For the Rayleigh–Bénard convection studied here we perform a KLD on the two-dimensional flow field pattern at the mid-plane as shown in Fig. 1. The reason for this is twofold. One, a typical experiment using shadowgraphy to measure the convective roll pattern would generate the same type of data [19]. Second, it is expected that the convection rolls do not contain structure in the vertical direction that would have a significant impact upon the dimension. In collecting data for our KLD we use images from the flow field separated in time by $5\tau_v$ where the total duration of the numerical simulation depends upon the system size explored.

2.2.1. Approach (i)

The size of the eigenvalue problem to solve the Fredholm integral in Eq. (9) is large. The scale of the computations can be reduced using the method of snapshots [28]. The method of snapshots recasts the eigenfunction in the Fredholm integral in Eq. (9) as a linear combination of the snapshots where

$$c(t) = \int_{\Omega} \mathbf{u}(\mathbf{x}', t)\mathbf{\Phi}(\mathbf{x}')d^3x' \tag{12}$$

and Eq. (9) is then

$$\lim_{\tau\to\infty} \frac{1}{\tau} \int_0^{\tau} \mathbf{u}(\mathbf{x}, t)c(t)dt = \mu\mathbf{\Phi}(\mathbf{x}). \tag{13}$$

Multiplying both sides by $\mathbf{u}(\mathbf{x}, t')$ and integrating yields,

$$\lim_{\tau\to\infty} \frac{1}{\tau} \int_0^{\tau} c(t) \int_{\Omega} \mathbf{u}(\mathbf{x}, t')\mathbf{u}(\mathbf{x}, t)\, d^3x\, dt = \mu c(t') \tag{14}$$

or

$$\lim_{\tau\to\infty} \frac{1}{\tau} \int_0^{\tau} (\mathbf{u}(\mathbf{x}, t'), \mathbf{u}(\mathbf{x}, t))c(t)\, dt = \mu c(t') \tag{15}$$

where $(,)$ denotes an inner product over the domain Ω. The resulting equation is now a Fredholm integral in time. In fluid dynamics this is more computationally tractable because there are typically fewer time observations (snapshots) than there are spatial observations (grid points).

2.2.2. Approach (ii)

For a rotationally invariant system every rotation of the solution is also valid. The coefficients of the KLD in the azimuthal direction are therefore those of a Fourier series [29]. In this case, the eigenmode for mode m,

$$\mathbf{\Phi}_m(r, \theta) = \mathbf{\Psi}_n^q(r)e^{in\theta}, \tag{16}$$

is uniquely described with an azimuthal wavenumber n and eigen number q. This reduces the computation of the Karhunen–Loève modes to

$$\int_0^{r_0} \mathscr{K}_n(r, r')\mathbf{\Psi}_n(r')r'dr' = \mu_n\mathbf{\Psi}_n(r), \tag{17}$$

where

$$\mathscr{K}_n(r, r') = \lim_{\tau\to\infty} \frac{1}{\tau} \int_0^{\tau} \hat{\mathbf{u}}_n(r, t) \otimes \hat{\mathbf{u}}_n^{\star}(r', t)\, dt, \tag{18}$$

with $\star$ denoting the complex conjugate and the weight r' is present because the inner product is evaluated in polar-cylindrical coordinates (r, θ). The Fourier transform of the velocity in the azimuthal direction is $\hat{\mathbf{u}}_n(r, t)$. The kernel in Eq. (17) is Hermitian as it was in Eq. (9) and yields real and positive eigenvalues. Using a Q-point quadrature to solve Eq. (17) yields $3Q$ eigenvectors and corresponding eigenvalues in descending order for each azimuthal mode n, denoted with eigen number q. Physically, each eigenvector $\mathbf{\Psi}_n^q(r)e^{in\theta}$ represents a velocity field and the eigenvalue μ_n^q is the time averaged energy of that flow field.

3. Discussion

3.1. Computing the Karhunen–Loève dimension

We now illustrate the differences in our two approaches for computing D_{KL} through two examples using numerical data from our simulations for $\Gamma = 10$. In the first example we compute the dimension using four flow field images. In the second example, we compute the dimension using a single flow field image that is rotated azimuthally.

The flow field patterns from four instances in time separated by $50\tau_v$ are shown in Fig. 2. Approach (i) yields a dimension of $D_{KL} = 3.49$ when using all four images. However, using Approach (ii) the dimensions of the individual images are $D_{KL} = 46.1, 46.8, 49.8, 48.5$ for panels (a)–(d), respectively. If we construct a time series out of these images and compute the dimension using images from panels (a), (a and b), (a–c), and (a–d) we find the values of the cumulative dimension as shown in Table 1. The magnitude of the dimension increases rapidly with the addition of each new flow field image. When using all four images Approach (ii) yields a dimension of $D_{KL} = 147.4$ which is less than the sum of the individual contributions 191.2. This example demonstrates that the rate at which the two approaches attain an asymptotic value of the dimension is quite different. It is clear that Approach (ii) is quite useful for systems with large dimensions.

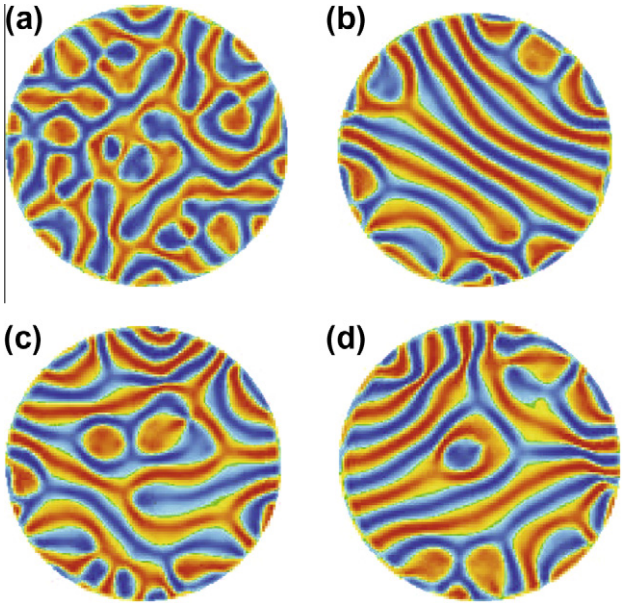

Fig. 2. Four flow fields from numerical simulation that are separated in time by $50\tau_v$ for $\Gamma = 10$, $R/R_c = 3.5$, $\sigma = 1$. The values of D_{KL} computed using Approach (ii) for each individual flow field are 46.1, 46.8, 49.8, and 48.5 for panels (a)–(d), respectively.

Table 1
The cumulative Karhunen–Loève dimension of the four flow field images shown in Fig. 2. The number of images used in computing the dimension is n for both approaches (i) and (ii).

Samples, n	Approach (i), D_{KL}	Approach (ii), D_{KL}
1	0.9	46.1
2	1.79	84.2
3	2.64	118.3
4	3.49	147.4

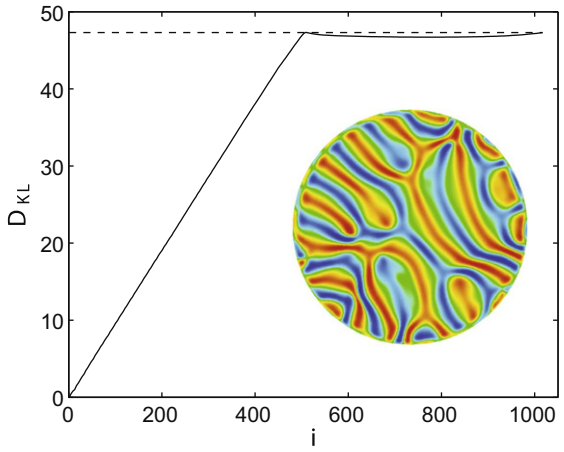

Fig. 3. The cumulative dimension of a flow field pattern where a single flow field image is rotated azimuthally by increments of $\Delta\theta = 2\pi/512$ to form new images where the angle of rotation is $\theta_i = i\Delta\theta$ and i is an integer. Results are shown for a total of 1024 rotations where Approach (i) is the solid line and Approach (ii) is the dashed line. The two approaches agree when $i = 512$ and 1024 corresponding to one and two complete rotations of the flow field, respectively. The flow field used is at time $t = 500$ (see inset) and for the simulation parameters $\Gamma = 10$, $\sigma = 1$, and $R/R_c = 3.5$.

Using the same convection domain with $\Gamma = 10$ we now consider a single flow field image from time $t = 500$ that is rotated azimuthally in small increments to create a series of images that is then used to compute D_{KL}. The specific flow field pattern that is used is shown in the inset of Fig. 3. The image is rotated incrementally by $\Delta\theta = 2\pi/512$ to yield rotations of $\theta = i\Delta\theta$ where $i = 1, 2, \ldots, 1024$ resulting in two complete rotations.

The values of D_{KL} for the two approaches are shown in Fig. 3. The dimension from Approach (ii) is $D_{KL} = 47.3$ using only one image and remains at this value for the subsequent incremental rotations. Approach (i) however, increases monotonically for each incremental rotation and agrees with Approach (ii) only after one complete rotation. This occurs for subsequent complete rotations as well.

This example illustrates the computational advantage of Approach (ii) for computing D_{KL} in the limit of a system with rotational invariance. It also shows that the two approaches eventually yield the same value for D_{KL}. The computed values of D_{KL} only agree after the flow field pattern has undergone a complete rotation. For the case of actual flow field data, it is expected that the two approaches would also agree if enough data were used for Approach (i) to sample from all of the possible orientations [14]. However, this can be a very slow process as we will demonstrate.

3.2. The Lyapunov and Karhunen–Loève dimensions

A significant advantage of studying chaotic Rayleigh–Bénard convection is that the spectrum of Lyapunov exponents has been calculated to yield quantitative measurements of the Lyapunov dimension [30,31]. The spectrum of Lyapunov exponents λ_j measure the exponential separation of trajectories in phase space and are ordered from largest to smallest. A single positive exponent is the defining feature of deterministic chaos (cf. [1,32,33]). The sum of the first N exponents indicates the exponential growth of an N-dimensional ball of initial conditions in phase space.

The number of exponents that must be added in order for their sum to equal zero yields the Lyapunov dimension. Using a linear interpolation to find the precise value of this number is the commonly used Kaplan–Yorke formula [34],

$$D_\lambda = J + \frac{S_J}{|\lambda_{J+1}|}, \tag{19}$$

where J is the largest j for which

$$S_J = \sum_{j=1}^{J} \lambda_j > 0. \tag{20}$$

The Lyapunov dimension D_λ is an approximation to the number of degrees of freedom that contribute to the chaotic dynamics [35,1].

The Karhunen–Loève dimension was compared with the Lyapunov dimension by Sirovich and Deane [36] as the Rayleigh number was varied for turbulent Rayleigh–Bénard convection in a small periodic domain with free surface boundary conditions. Zoldi et al. [37] computed D_{KL} from experimental shadowgraph images of the spiral defect chaos state [38] of Rayleigh–Bénard convection in a large cylindrical domain with $\Gamma = 109$. In order to explore the variation of D_{KL} with the system size the data was spatially sampled with a square window of increasing size. Using this approach it was found that D_{KL} scaled linearly with window size demonstrating extensivity. For Rayleigh–Bénard convection in a shallow layer there are effectively two spatially extended directions and, as a result, the system size is measured as Γ^{-2}.

The spiral defect chaos state has also been explored numerically. Using a range of large periodic box geometries D_λ was found to scale extensively with system size for $\Gamma = 48$, 56, 64 and $R/R_c = 1.8$ [30]. For box geometries the aspect ratio is defined as $\Gamma = L/d$, where L is the length of an entire side of the box. The dimension $D_\lambda \approx 80$ for the largest domain and the dimension density was found to be $\delta_\lambda = D_\lambda/\Gamma^2 \approx 0.019$. The extensivity of chaos was also shown numerically for a range of finite cylindrical geometries for $4.72 \leqslant \Gamma \leqslant 15$, $\sigma = 1$, and $R/R_c = 3.5$ [31]. In this case the dimension density was found to be $\delta_\lambda \approx 0.25$. In our study we have chosen to explore the same system parameters as those of Ref. [31] and to compute the variation of D_{KL} over the same range of system sizes.

3.3. Eigenvalues and eigenfunctions

We next examine the approach of the eigenvalues to their asymptotic values. The normalized eigenvalue distribution is given by

$$\eta_i = \frac{\mu_i}{\sum_i \mu_i}, \tag{21}$$

where the index i is over all computed eigenvalues μ_i. The variation in the magnitude of the error with time $E_\eta(\tau)$ is computed as,

$$E_\eta(\tau) = 1 - \frac{|\eta_i(\tau)|}{|\eta_{i,\infty}|}, \tag{22}$$

where $|\eta_i|$ is the magnitude of the eigenvalue spectrum and $|\eta_{i,\infty}|$ is the value using the largest τ available for each case. The error E_η decreases rapidly with time and is shown in Fig. 4. The time has been normalized by the nondimensional time required for heat to diffuse a distance r_0 which we refer to as the horizontal diffusion time $\tau_h = \Gamma^{-2}$. The nondimensional time scale of the fluid motion in a convection roll is on the order of $\tau \approx 1$ and τ_h represents a long-time scale.

The rate at which Approach (ii) attains its asymptotic value is found to be faster than Approach (i). For example, for $\tau \approx 5\tau_h$ the error is $E_\eta \sim 10^{-2}$ using Approach (i) whereas $E_\eta \sim 10^{-4}$ using Approach (ii).

The approach of the KLD modes to their asymptotic values depend upon their eigenvalue. Fig. 5 shows the variation of modes 1, 25, and 50 with increasing time. Again we use the data for the largest available τ as an approximation for $\tau \to \infty$. The time variation of the magnitude of the error for the ith mode is computed as

$$E_{\Phi,i}(\tau) = 1 - \frac{(\mathbf{\Phi}_i(\tau), \mathbf{\Phi}_{i,\infty})}{(\mathbf{\Phi}_{i,\infty}, \mathbf{\Phi}_{i,\infty})}. \tag{23}$$

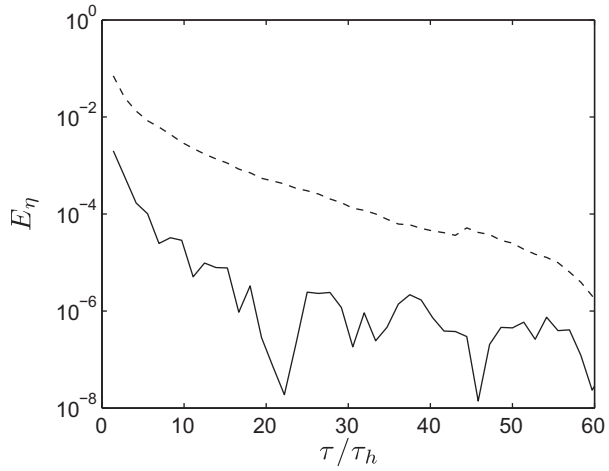

Fig. 4. The approach of the normalized eigenvalue spectrum to its asymptotic value as a function of time τ for $\Gamma = 6$. The time has been normalized by the horizontal diffusion time τ_h. The error is given by E_η for Approach (i) (dashed line) and Approach (ii) (solid line) using Eq. (22).

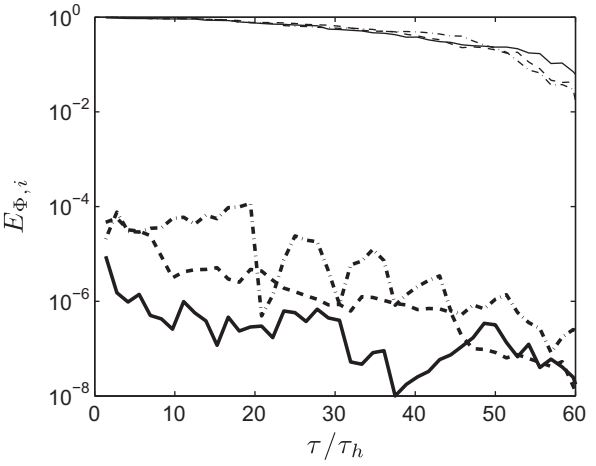

Fig. 5. The approach of the eigenfunctions to their asymptotic values with time for a convection domain with aspect ratio $\Gamma = 6$. The error in the eigenfunction for mode i is given by $E_{\Phi,i}$ in Eq. (23). Results are shown for $i = 1$ (solid lines), $i = 25$ (dashed lines), and $i = 50$ (dash-dotted lines). The results computed using Approach (i) are represented by thin lines and those using Approach (ii) are represented by thick lines.

Again, Approach (ii) attains the asymptotic value faster than Approach (i).

3.4. The Karhunen–Loève dimension

The variation of D_{KL} for $\Gamma = 6$ with respect to time is shown in Fig. 6. where the time has been scaled by the horizontal diffusion time τ_h. Results are given for both approaches (i) and (ii). Approach (ii) has reached a value of $D_{\mathrm{KL}} \approx 142$ after $\tau \approx 20\tau_h$.

On the other hand, Approach (i) exhibits a very gradual convergence. The numerical simulations were continued until $\tau \approx 60\tau_h$. In order to estimate a value of the asymptotic value of the dimension D_∞ for Approach (ii) the results are fit with the following exponential dependence,

$$D_{\mathrm{KL}}(\tau) = D_\infty + c_1 e^{-c_2\tau/\tau_h} + c_3 e^{-c_4\tau/\tau_h}, \tag{24}$$

where c_1, c_2, c_3, and c_4 are constants and the fit is shown by the dashed line. The fitted curve is used to determine the asymptotic value of the dimension to yield $D_\infty = 137.8$ and is indicated by the solid line.

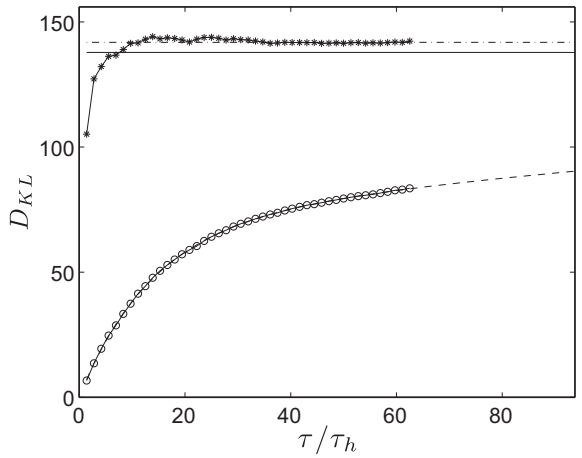

Fig. 6. The variation of D_{KL} with time for Approach (ii) (stars) and Approach (i) (circles) for $\Gamma = 6$. The long-time asymptotic value for Approach (ii) is given by the dash-dotted line. The curve fit for Approach (i) is $D_{\mathrm{KL}} = 137.8 - 68.4\exp(-0.0730\tau/\tau_h) - 69.3\exp(-0.00406\tau/\tau_h)$ and is given by the dashed line. The asymptotic value of the dimension for Approach (i) is given by the solid line at $D_\infty = 137.8$.

For the dimension to converge within 10% of D_∞ requires a time of $\tau \sim 400\tau_h$. Such a slow convergence rate in time is typical of our results for Approach (i). A further difficulty resulting from the slow convergence is the that the value of D_∞ is very sensitive to small variations in the data that is made more significant when only a finite amount of data is available. The variation of D_{KL} with time is shown for $\Gamma = 10$, 12, 15 in Figs. 7–9, respectively, and numerical values of the D_{KL} are given in Table 2.

3.5. Extensivity

Fig. 10 shows the time variation of the cumulative normalized energy of the first N eigenvalues. The normalized energy is computed from,

$$E_N(\tau) = \frac{\sum_{k=0}^{N}\mu_k}{\sum_{k=0}^{\infty}\mu_k} \tag{25}$$

using the data from Approach (ii) with the largest τ for each respective system size. The basic trend of $E_N(\tau)$ shows that the total num-

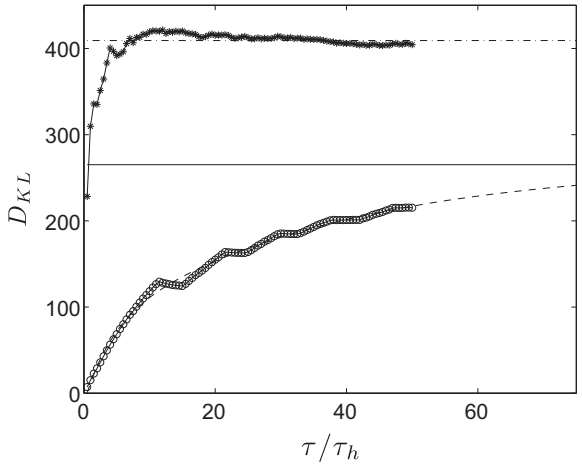

Fig. 7. The variation of D_{KL} with time τ for Approach (ii) (stars) and Approach (i) (circles) for $\Gamma = 10$. The long-time asymptotic value for Approach (ii) is given by the dash-dotted line. The curve fit for Approach (i) is $D_{\mathrm{KL}}(\tau) = 265.2 - 82.0\exp(-0.2455\tau/\tau_h) - 194.8\exp(-0.02796\tau/\tau_h)$ and is given by the dashed line. The asymptotic value of the dimension for Approach (i) is given by the solid line at $D_\infty = 265.2$.

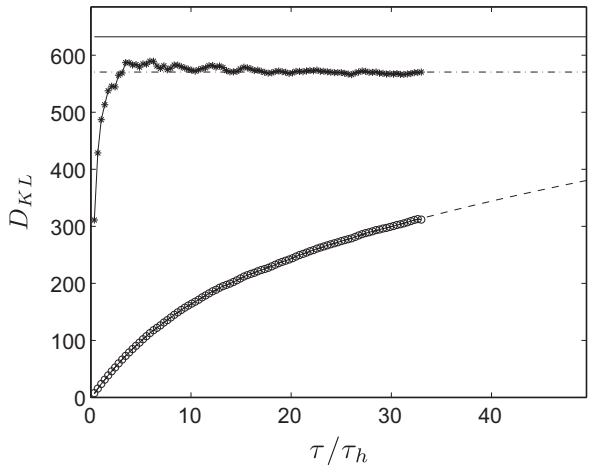

Fig. 8. The variation of D_{KL} with time τ for Approach (ii) (stars) and Approach (i) (circles) for $\Gamma = 12$. The long-time asymptotic value for Approach (ii) is given by the dash-dotted line. The curve fit for Approach (i) is $D_{KL}(\tau) = 632.2 - 130.6\exp(-0.1444\tau/\tau_h) - 504.2\exp(-0.01404\tau/\tau_h)$ and is given by the dashed line. The asymptotic value of the dimension for Approach (i) is given by the solid line at $D_\infty = 632.2$.

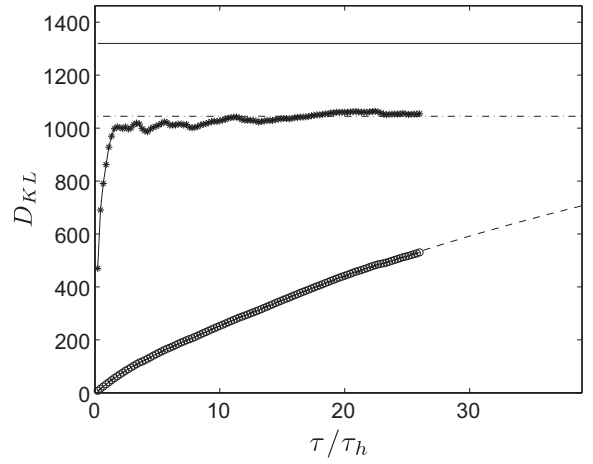

Fig. 9. The variation of D_{KL} with time τ for Approach (ii) (stars) and Approach (i) (circles) for $\Gamma = 15$. The long-time asymptotic value for Approach (ii) is given by the dash-dotted line. The curve fit for Approach (i) is $D_{KL}(\tau) = 1320.1 - 36.5\exp(-0.7892\tau/\tau_h) - 1290.3\exp(-0.01908\ \tau/\tau_h)$ and is given by the dashed line. The asymptotic value of the dimension for the Approach (i) is given by the solid line at $D_\infty = 1320.1$.

Table 2
The variation of the dimension with system size. The asymptotic values of the Karhunen–Loève dimension D_∞ are given for both approaches (i) and (ii). The Lyapunov dimension D_λ computed for the same system parameters are included from Ref. [31].

Γ	Approach (i), D_{KL}	Approach (ii), D_{KL}	Lyapunov, D_λ
6	138	142	6.8
10	265	409	21.6
12	632	570	32.5
15	1320	1045	53.7

ber of modes N needed to capture a fraction f increases with system size. Fig. 11 shows the variation of D_{KL} with system size using different values of f where $0.5 \leqslant f \leqslant 0.95$. Our results yield a linear relationship between D_{KL} and Γ^2 over the entire range. The choice for D_{KL} that we have used for reporting values of D_{KL} is $f = 0.9$.

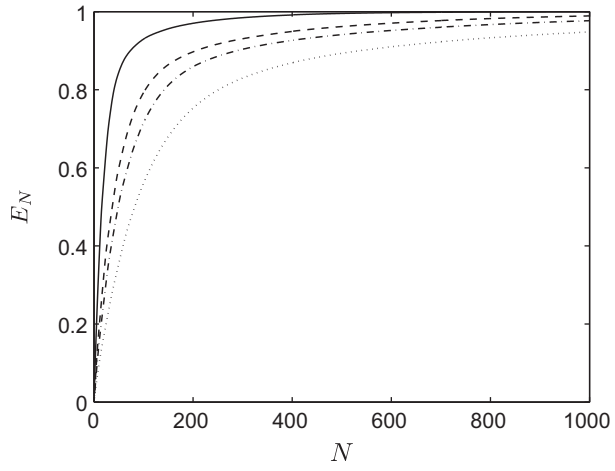

Fig. 10. The fraction of the total energy captured E_N as a function of the number of modes N using Approach (ii). Results are shown for $\Gamma = 6$ (solid line), $\Gamma = 10$ (dashed line), $\Gamma = 12$ (dash-dotted line), and $\Gamma = 15$ (dotted line). A typical approach used to compute the value of D_{KL} is to use the number of modes needed for $E_N = 0.9$. From these results it is clear that D_{KL} increases in value as the system size is increased.

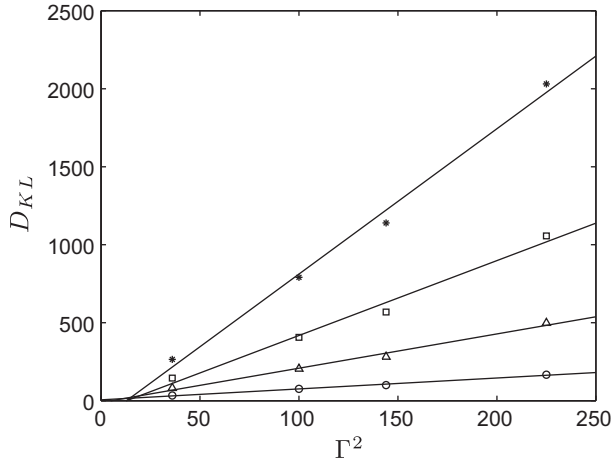

Fig. 11. The variation of the dimension D_{KL} with system size Γ^2 for several choices of f using Approach (ii). Results are shown for $f = 0.5$ (circles), $f = 0.8$ (triangles), $f = 0.9$ (squares), and $f = 0.95$ (stars). The solid lines are linear curve fits through the data indicating the extensivity of D_{KL}. In the following figures we have chosen to use $f = 0.9$ when reporting values of D_{KL}.

The variation of D_{KL} with system size is shown in Fig. 12 using Approach (ii) (squares) and Approach (i) (triangles) and linear curve fits through the data are given by the solid line and the dash-dotted line, respectively. The results using Approach (i) increase with system size but with significant deviations from the line of extensivity. As discussed, the approach to the asymptotic value for Approach (i) is very slow and our numerical results would need to be continued for much longer simulation times for these results to converge. However, if this were done it is anticipated that the results would eventually agree with those of Approach (ii) which is extensive.

The variation of D_λ with system size is shown in Fig. 12 by the circles with a linear curve fit given by the dashed line. Although there is no reason to expect the two dimensions to be related since they measure very different aspects of the patterns and their dynamics, it has been suggested that for extensively chaotic dynamics their rate of increase should be similar [39]. Numerical values of the dimensions are given in Table 2. Using the linear curve fits through the data yields the relationship $D_{KL} \approx 19.7 D_\lambda$.

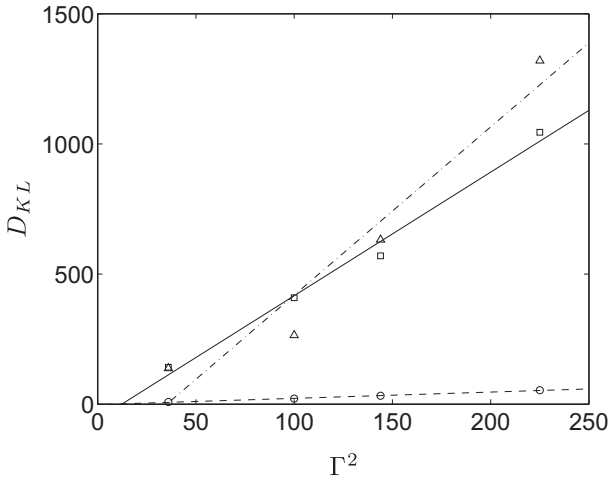

Fig. 12. The variation of D_{KL} and D_λ with system size Γ^2 using numerical results for $\Gamma = 6$, 10, 12 and 15. The values of D_{KL} computed using Approach (ii) are represented as squares and the solid line is a linear curve fit. The value of D_{KL} computed using Approach (i) are represented as triangles and the dash-dot line is a linear curve fit. The Lyapunov dimension from Ref. [31] are represented as circles and the dashed line is a linear curve fit. From the data $D_{KL} \approx 19.7 D_\lambda$ where Approach (ii) has been used for D_{KL}.

4. Conclusions

We have performed a Karhunen–Loève decomposition on a finite cylindrical domain containing a shallow fluid layer undergoing extensively chaotic dynamics. Our results suggest that even for this case the required time necessary to obtain good estimates of the Karhunen–Loève dimension is very long and on the order of hundreds of horizontal diffusion times. However, by exploiting the rotational symmetry of the problem the time to convergence can be drastically reduced using Approach (ii). This has important consequences for more complex flow fields that are common in engineering applications where the amount of data available is limited in both experiment and for computations. A prime example is the use of particle image velocimetry to obtain detailed information about the flow field. In this case the observation time is a function of the amount of data that can be captured by the camera. Overall, our results show that one must be careful in order to obtain an accurate estimation of the asymptotic value of the Karhunen–Loève dimension.

Acknowledgments

This computations were conducted using the resources of the National Science Foundation TeraGrid and the Advanced Research Computing center at Virginia Tech. M.R.P. acknowledges support from NSF Grant No. CBET-0747727. We also gratefully acknowledge useful interactions with Paul Fischer and Mike Cross.

References

[1] Cross MC, Hohenberg PC. Pattern formation outside of equilibrium. Rev Mod Phys 1993;65(3 II):851–1112.
[2] Lumley JL. The structure of inhomogeneous turbulent flows. Moscow: Nauka; 1967.
[3] Sirovich L. Turbulence and the dynamics of coherent structures, part I: coherent structures. Quart Appl Math 1987;XLV(3):561–71.
[4] Sirovich L. Turbulence and the dynamics of coherent structures, part II: symmetries and transformations. Quart Appl Math 1987;XLV(3):573–82.
[5] Sirovich L. Turbulence and the dynamics of coherent structures, part III: dynamics and scaling. Quart Appl Math 1987;XLV(3):583–90.
[6] Sirovich L. Chaotic dynamics of coherent structures. Physica D 1989;37:126.
[7] Sirovich L, Ball KS, Keefe LR. Plane waves and structures in turbulent channel flow. Phys Fluids A 1990;12:2217–26.
[8] Sirovich L, Ball KS, Handler RA. Propagating structures in wall-bounded turbulent flows. Theor Comput Fluid Dyn 1991;2:307.
[9] Ball KS, Sirovich L, Keefe LR. Dynamical eigenfunction decomposition of turbulent channel flow. Int J Numer Methods Fluids 1991;12:587.
[10] Duggleby A, Ball KS, Paul MR, Fischer PF. Dynamical eigenfunction decomposition of turbulent pipe flow. J Turbul 2007;8(43).
[11] Duggleby A, Ball KS, Schwaenen M. Structure and dynamics of low reynolds number turbulent pipe flow. Phil Trans Roy Soc A 2009;347:473–88.
[12] Webber GA, Handler RA, Sirovich L. Energy dynamics in a turbulent channel flow using the Karhunen–Loève approach. Int J Numer Methods Fluids 2002;40:1381–400.
[13] Zhou X, Sirovich L. Coherence and chaos in a model of the turbulent boundary layer. Phys Fluids A 1994;4:2955–74.
[14] Handler RA, Housiadas KD, Beris AN. Karhunen–Loève representations of turbulent channel flows using the method of snapshots. Int J Numer Methods Fluids 2006;52(12):1339–60.
[15] Housiadas KD, Beris AN, Handler RA. Viscoelastic effects on higher order statistics and on coherent structures in turbulent channel flow. Phys Fluids 2005;17(3).
[16] Duggleby A, Ball KS, Paul MR. The effect of spanwise wall oscillation on turbulent pipe flow structures resulting in drag reduction. Phys Fluids 2007;19(125107).
[17] Lian Y, Shyy W, Vileru D, Zhang B. Membrane wing aerodynamics for micro air vehicles. Prog Aero Sci 2003;39(6–7):425–65.
[18] Epureanu B, Hall K, Dowell E. Reduced-order models of unsteady viscous flows in turbomachinery using viscous-inviscid coupling. J Fluids Struct 2001;15(2):255–73.
[19] Bodenschatz E, Pesch W, Ahlers G. Recent developments in Rayleigh–Bénard convection. Annu Rev Fluid Mech 2000;32:709–78.
[20] Ahlers G. Low temperature studies of the Rayleigh–Bénard instability and turbulence. Phys Rev Lett 1974;33(20):1185–8.
[21] Libchaber A, Maurer J. Local probe in a Rayleigh–Bénard experiment in liquid helium. J Phys Lett 1978;39:369–72.
[22] Pocheau A. Transition to turbulence of convective flows in a cylindrical container. J Phys France 1988;49:1127–45.
[23] Paul MR, Cross MC, Fischer PF, Greenside HS. Power-law behavior of power spectra in low Prandtl number Rayleigh–Bénard convection. Phys Rev Lett 2001;87(15):154501.
[24] Fischer P, Patera A. Parallel simulation of viscous incompressible flows. Annu Rev Fluid Mech 1994;26:483–527.
[25] Fischer PF. An overlapping Schwarz method for spectral element solution of the incompressible Navier–Stokes equations. J Comput Phys 1997;133:84–101.
[26] Tufo HM, Fischer PF. Terascale spectral element algorithms and implementations. In: Proceedings of the ACM/IEEE SC99 Conference on High Performance Networking and Computing. IEEE Computer Society; 1999 [Gordon Bell Prize paper].
[27] Paul MR, Chiam K-H, Cross MC, Fischer PF, Greenside HS. Pattern formation and dynamics in Rayleigh–Bénard convection: numerical simulations of experimentally realistic geometries. Physica D 2003;184:114–26.
[28] Sirovich L, Kirby M. Low-dimensional procedure for the characterization of human faces. J Opt Soc Am A 1987;4(3):519–24.
[29] Holmes P, Lumley JL, Berkooz G. Turbulence, coherent structures, dynamical systems, and symmetry. Cambridge, UK: Cambridge University Press; 1996.
[30] Egolf DA, Melnikov IV, Pesch W, Ecke RE. Mechanisms of extensive spatiotemporal chaos in Rayleigh–Bénard convection. Nature 2000;404:733–6.
[31] Paul MR, Einarsson MI, Cross M, Fischer P. Extensive chaos in Rayleigh–Bénard convection. Phys Rev E 2007;75(045203).
[32] Eckmann JP, Ruelle D. Ergodic theory of chaos and strange attractors. Rev Mod Phys 1985;57(3):617–56.
[33] Wolf A, Swift J, Swinney HL, Vastano A. Determining Lyapunov exponents from a time series. Physica D 1985;16:285–317.
[34] Kaplan J, Yorke J. Chaotic behavior in multi-dimensional difference equations. In: Functional differential equations and the approximation of fixed points. Lecture Notes in Mathematics, vol. 730. Springer; 1979. p. 228.
[35] Farmer JD, Ott E, Yorke JA. The dimension of chaotic attractors. Physica 7D 1983:153–80.
[36] Sirovich L, Deane AE. A computational study of Rayleigh–Bénard convection. Part 2. Dimension considerations. J. Fluid Mech. 1991;222:251–65.
[37] Zoldi SM, Liu J, Bajaj KMS, Greenside HS, Ahlers G. Extensive scaling and nonuniformity of the Karhunen–Loè decomposition for the spiral-defect chaos state. Phys. Rev. E 1998;58(6):R6903–6.
[38] Morris SW, Bodenschatz E, Cannell DS, Ahlers G. Spiral defect chaos in large aspect ratio Rayleigh–Bénard convection. Phys Rev Lett 1993;71(13):2026–9.
[39] Zoldi SM, Greenside HS. Karhunen–Loève decomposition of extensive chaos. Phys Rev Lett 1997;78(9):1687–90.